J. Fluid Mech. (2008), *vol.* 609, *pp.* 195–220.
doi:10.1017/S0022112008002541 Printed in the United Kingdom

Statistical structure of the fluctuating wall pressure and its in-plane gradients at high Reynolds number

J. C. KLEWICKI[1], P. J. A. PRIYADARSHANA[1] AND M. M. METZGER[2]

[1]Department of Mechanical Engineering, University of New Hampshire, Durham, NH 03824, USA
[2]Department of Mechanical Engineering, University of Utah, Salt Lake City, UT 84112, USA

(Received 16 November 2007 and in revised form 13 May 2008)

The fluctuating wall pressure and its gradients in the plane of the surface were measured beneath the turbulent boundary layer that forms over the salt playa of Utah's west desert. Measurements were acquired under the condition of near-neutral thermal stability to best mimic the canonical zero-pressure-gradient boundary-layer flow. The Reynolds number (based on surface-layer thickness, δ, and the friction velocity, u_τ) was estimated to be $1 \times 10^6 \pm 2 \times 10^5$. The equivalent sandgrain surface roughness was estimated to be in the range $15 \leqslant k_s^+ \leqslant 85$. Pressure measurements acquired simultaneously from an array of up to ten microphones were analysed. A compact array of four microphones was used to estimate the instantaneous streamwise and spanwise gradients of the surface pressure. Owing to the large length scales and low flow speeds, attaining accurate pressure statistics in the present flow required sensors capable of measuring unusually low frequencies. The effects of imperfect spatial and temporal resolution on the present measurements were also explored. Relative to pressure, pressure gradients exhibit an enhanced sensitivity to spatial resolution. Their accurate measurement does not, however, require fully capturing the low frequencies that are inherent and significant in the pressure itself. The present pressure spectra convincingly exhibit over three decades of approximately -1 slope. Comparisons with low-Reynolds-number data support previous predictions that the inner normalized wall pressure variance increases logarithmically with Reynolds number. The wall pressure autocorrelation exhibits its first zero-crossing at an advected length that is between one tenth and one fifth of the surface-layer thickness. Under any of the normalizations investigated, the present surface vorticity flux intensity values are difficult to reconcile with low-Reynolds-number data trends. Inner variables, however, do yield normalized flux intensity values that are of the same order of magnitude at low and high Reynolds number. Spectra reveal that even at high Reynolds number, the primary contributions to the pressure gradient intensities occur over a relatively narrow frequency range. This frequency range is shown to be consistent with the scale of the sublayer pocket motions. In accord with low-Reynolds-number data, the streamwise pressure gradient signals at high Reynolds number are also characterized by statistically significant pairings of opposing sign fluctuations.

1. Introduction

The objectives of this study are to explore the statistical properties of the wall pressure fluctuations and their in-plane gradients beneath a high-Reynolds-number

boundary layer. (The Reynolds number primarily employed herein is based upon the boundary-layer thickness, δ, and the friction velocity, $u_\tau = \sqrt{\tau_w/\rho}$, i.e. $\delta^+ = \delta u_\tau/\nu$, where ν is the kinematic viscosity.) Efforts to reveal the detailed nature of high-Reynolds-number boundary-layer turbulence encounter a number of technical challenges. Beyond those associated with actually generating a high δ^+ boundary layer, these challenges primarily relate to measuring the small scales and high frequencies of the turbulent motions (e.g. DeGraaff & Eaton 2000; Metzger & Klewicki 2001). This is because the most common way to achieve a high Reynolds number in the laboratory is to operate at high speeds. Regarding wall pressure, additional challenges are associated with the non-negligible acoustic noise and facility vibration typical of even high-flow-quality wind tunnels. These complications often require considerable data post-processing to extract reliable estimates of the true wall-pressure signal. Similarly, the signal-to-noise ratios of wall-pressure signals are often not as high as desired – especially for studies seeking to estimate derivatives. Thus, for example, even theoretically 'well-established' features of the wall-pressure fluctuations, such as the k^{-1} spectral range, are often difficult to convincingly verify experimentally, (Panton 1990).

There is a well-established theoretical foundation regarding the source of pressure fluctuations within the boundary layer (e.g. Blake 1986). Physically, unsteady wall-pressure signals arise from the weighted integral of the instantaneous motions internal to the turbulent boundary layer (e.g. Eckelmann 1990). Understanding the nature and origin of these pressure sources is central to applications associated, for example, with the acoustic signature of submarines or high-speed aircraft. As it pertains to the present effort, these two high-Reynolds-number applications are particularly relevant, since high-fidelity wall-pressure measurements that are also spatially and temporally well-resolved do not exist above moderate Reynolds numbers. Existing high-quality wind-tunnel measurements are, to our knowledge, almost exclusively confined to Reynolds numbers less than $\delta^+ \approx 1 \times 10^4$ (Farabee & Casarella 1991; Tsuji *et al.* 2007). Furthermore, only a subset of existing measurements used sensors having a normalized sensor diameter ($d^+ = du_\tau/\nu$) less than about 50.

Evaluating the Navier–Stokes equation at a planar surface (herein taken to be the x, z plane at $y = 0$) reveals that the instantaneous flux of vorticity from the surface is directly related to the gradients of pressure in the plane of the surface (Lighthill 1963). Specifically, evaluation of the streamwise, x, momentum equation at the surface leads to a relation between $\partial\tilde{p}/\partial x$ and the flux of spanwise vorticity, $\tilde{\omega}_z$ (tilde denoting an instantaneous quantity, e.g. $\tilde{p} = P + p$) (note that for the present flow $\partial\tilde{p}/\partial x = \partial p/\partial x$ and $\partial\tilde{p}/\partial z = \partial p/\partial z$).

$$\frac{\partial\tilde{p}}{\partial x} = -\mu\frac{\partial\tilde{\omega}_z}{\partial y}. \tag{1.1}$$

Similarly, evaluation of the spanwise, z, momentum equation yields a relation between $\partial\tilde{p}/\partial z$ and the flux of streamwise vorticity, $\tilde{\omega}_x$,

$$\frac{\partial\tilde{p}}{\partial z} = \mu\frac{\partial\tilde{\omega}_x}{\partial y}. \tag{1.2}$$

Time-resolved surface pressure gradient data are considerably more scarce than pressure data. Previously reported surface pressure gradient results are exclusively from Andreopolous and co-workers, e.g. Andreopoulos & Agui (1996) and Honkan & Andreopoulos (1997), who explored turbulent boundary-layer surface vorticity fluxes over the range $1300 \leqslant \delta^+ \leqslant 2900$. In these studies, they employed a square array

of four flush-mounted microphones to obtain pressure fluctuation signals at four adjacent points in the plane of the surface. The resulting simultaneous signals were then differenced to estimate the streamwise and spanwise gradients of pressure. A particularly notable and somewhat surprising result of these studies is that over the indicated δ^+ range both $(\partial\omega_x^+/\partial y^+)_{rms}$ and $(\partial\omega_z^+/\partial y^+)_{rms}$ exhibit a decrease from a value near 0.065 to a value of about 0.02. These same data show only minimal variation over the same range of δ^+ when normalized using θ and u_τ.

Further analyses by Andreopoulos & Agui (1996) also revealed that the high-amplitude streamwise wall-vorticity flux fluctuations are correlated with high-amplitude wall-pressure fluctuations, as well as with bipolar spanwise vorticity flux fluctuations. This latter result led to the conclusion that the associated characteristic vortical motions are mushroom shaped, and thus may have a connection to observations indicating the existence of adjacent regions of positive and negative spanwise vorticity in turbulent wall layers (e.g. Falco 1991; Klewicki *et al.* 1990; Klewicki 1997; Klewicki & Hill 1998; Klewicki & Hirschi 2004; Wu & Christensen 2006; Natrajan, Wu & Christensen 2007).

The brief review above reveals that the understanding of both the wall pressure and wall-pressure gradients would benefit from well-resolved data at large δ^+. In the present study, the characteristics of these pressure related quantities are studied at $\delta^+ \approx 10^6$. This is accomplished by probing the surface pressure fluctuations associated with the near neutral atmospheric surface-layer flow over the salt playa of western Utah, USA. The present results contribute to the understanding of boundary-layer surface pressure by providing high-Reynolds-number high signal-to-noise ratio data from sensors having good spatial and temporal resolution. We additionally present well-resolved high signal-to-noise wall-pressure gradient statistics at Reynolds number over two orders of magnitude higher than previous studies.

2. Experimental considerations

2.1. *SLTEST facility*

Fluctuating wall pressure was measured beneath the turbulent boundary layer that devolops over the surface of the playa at the Surface Layer Turbulence and Environmental Science Test (SLTEST) facility located on the Dugway Proving Ground, Dugway, Utah, USA. This site is characterized by an extremely flat and homogeneous terrain with wind patterns that are often consistent from day-to-day (Metzger & Klewicki 2001; Klewicki & Metzger 2003; Priyadarshana & Klewicki 2004; Metzger, McKeon & Holmes 2007*a*). The SLTEST site environment is almost entirely free from undesirable acoustic noise sources and, of course, completely devoid of any facility vibration. The measurements presented herein were acquired during field experiments in late May and/or early June 2003, 2004 and 2005. During early summer, the moisture content of the playa produces maximal surface smoothness while maintaining a structural integrity sufficient to support humans and equipment. During measurement periods in the early evening the flow originated from the north and developed over a fetch of about 150 km.

2.2. *Experiment description and test conditions*

Most of the data presented herein were acquired simultaneously with the experiments of Priyadarshana & Klewicki (2004), Metzger (2006), Metzger *et al.* (2007*a*) and Morris *et al.* (2007), and thus the overall documentation of the existant flow conditions is considerable. The total duration of data runs selected for analysis is about 2.3 h.

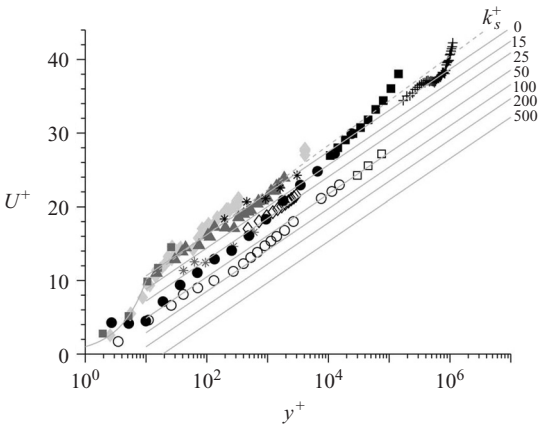

FIGURE 1. Inner normalized mean axial velocity profiles from hot-wire, sonic anemometry, PIV and minisodar data collected at SLTEST. ◆, Folz (1997); *, 6 element hot-wire (1999) in Priyadarshana & Klewicki (2004); ■, Metzger & Klewicki (2001); +, Metzger *et al.* (2001); ▲, hot-wire wall rake (2002); ○, hot-wire wall rake (2003); □, sonic anemometer (2003); ● ■, Metzger *et al.* (2007*a*); ◇, PIV Morris *et al.* (2007); –, log law using coefficients of Coles (1969); – –, log law using coefficients of Osterlund *et al.* (2000).

Arrays involving multiple microphones were, however, employed, and thus the total duration of the individual pressure time series analysed is larger by at least a factor of four. Statistics were computed for each data run and normalized using the friction velocity value measured during that run (e.g. see Priyadarshana *et al.* 2007). Statistics presented herein are the mean value of the ensemble of individual runs, and the error bars quantify the data scatter within the ensemble. The previous SLTEST studies cited above provide a detailed accounting of the data quality measures employed, and provide a listing of representative integral parameters that describe the surface-layer flow. During the acquistion runs, the average horizontal wind speed ranged from about 2.5 to 5.5 m s^{-1} at 2.5 m above the surface. Friction velocity values typically ranged between 0.2 and 0.35 m s^{-1} and the surface-layer thickness (δ) was estimated to fall generally in the range between 60 and 100 m.

Figure 1 shows near-surface inner normalized mean velocity data. Most of these were acquired during the same times as the present surface pressure experiments, but at adjacent locations at the SLTEST site. These data are derived from near-surface multisensor hot-wire probes, a vertical rake of hot-wire sensors, planar particle image velocimetry, a tower-based sonic anemometer array and a minisodar (Priyadarshana & Klewicki 2004; Metzger 2006; Metzger *et al.* 2007*a*; Morris *et al.* 2007). The data exhibit the expected logarithmic-like variation with distance from the surface, as well as a downward shift associated with surface roughness. From this downward shift, the equivalent sand grain roughness, k_s^+, was found to fall in the range $15 \leqslant k_s^+ \leqslant 85$ for all of the data runs considered herein. Mean velocity data derived from radiosonde and minisodar measurements indicate that the inner normalized boundary-layer thickness (top of the surface layer) varied in the range $8 \times 10^5 \lesssim \delta^+ \lesssim 1.2 \times 10^6$ (Priyadarshana & Klewicki 2004; Metzger *et al.* 2007*a*; Morris *et al.* 2007).

In order to best mimic isothermal flow conditions the measurements were acquired in the near-neutral thermal stability time period that generally occurs near sunset, between about 8:45 p.m. and 9:15 p.m. LST depending on the date. The influence of thermal stability was assessed through the use of the Monin–Obukhov stability

parameter, $\zeta = y/L$, where y is the distance from the surface and,

$$L = \frac{-u_\tau^3}{\kappa(g/\Theta_v)(\overline{v\theta_v})_w}, \tag{2.1}$$

is the Monin–Obukhov length. In this expression, the subscript w denotes that the quantity is evaluated in the immediate vicinity of the surface (according to meteorological convention this typically means at a position about 2 m from the surface), the overbar denotes time average, v and θ_v are the fluctuating vertical velocity and virtual potential temperature, respectively, Θ_v is the mean virtual potential temperature, κ is the von Kármán constant and u_τ is the friction velocity ($= \sqrt{\tau_w/\rho}$, where τ_w is the mean wall shear stress and ρ is the mass density). The condition $|\zeta = 1|$ is typically interpreted as the non-dimensional height above the surface where the buoyancy term and mechanical shear production term in the turbulence kinetic energy equation are balanced. Negative values of ζ indicate unstable thermal stratification, positive values indicate stable thermal stratification and $\zeta = 0$ is the condition of isothermal (neutrally stratified) flow. The data used in the present analyses were acquired in the early evening period during which ζ passed through zero. For the majority of these data the condition $|\zeta| \leqslant 0.1$ was satisfied.

Sonic anemometer based measurements of ζ were acquired at at 2 m, 3 m and 5 m above ground level. Example stability plots relevant to the acquistion times in 2004 and 2005 are given in Metzger *et al.* (2007*a*) and Morris *et al.* (2007). Previous measurements indicate that thermal stability effects on turbulence structure are undetectable to within the scatter of the data for a range of ζ near zero. Even more specifically, Metzger (2002) (also see Klewicki & Metzger 2003) has identified the time period near sunset during which ζ exhibits an approximately linear temporal dependence as the optimum time to acquire data containing minimal buoyancy effects. Additionally, numerous microphone measurement comparisons, acquired before and after the period of linear $\zeta(t)$, indicate that the surface pressure statistics and spectra are insensitive to small non-zero buoyancy effects. Under significantly unstable conditions, however, buoyancy-induced features begin to appear in the surface pressure spectra and autocorrelations.

The friction velocity ($u_\tau = \sqrt{\tau_w/\rho}$, where τ_w = wall shear stress) was estimated from a Reynolds stress measurement derived from a sonic anemometer positioned at 2 m from the surface. Previous data reveal that under near-neutral conditions these estimates are within about 10 % of those derived from a floating element drag plate (Sadr & Klewicki 2000; Metzger 2002). In calculating an estimate for u_τ, the kinematic viscosity ($\nu \simeq 1.85 \times 10^{-5}$) was computed from the density, as derived from the barometric pressure and temperature data, and from the dynamic viscosity, as tabulated as a function of temperature.

2.3. *Sensor resolution and signal characteristics*

2.3.1. *Resolving the wall pressure*

Fluctuating surface-pressure measurements were simultaneously acquired from up to ten microphones. One of the sensor configurations for experiments exploring sensor spatial and temporal resolution is depicted in figure 2. A set of hot-wire probes mounted at the rear of the measurement plate was also employed to acquire axial velocity data simultaneously. Results from these velocity sensors will be presented in a future paper. The wind vane situated atop the hot-wire stand was used to visually align the array. This vane, along with the rotatable circular plate, facilitated alignment prior to acquiring data for each run. Over the course of the study, a number

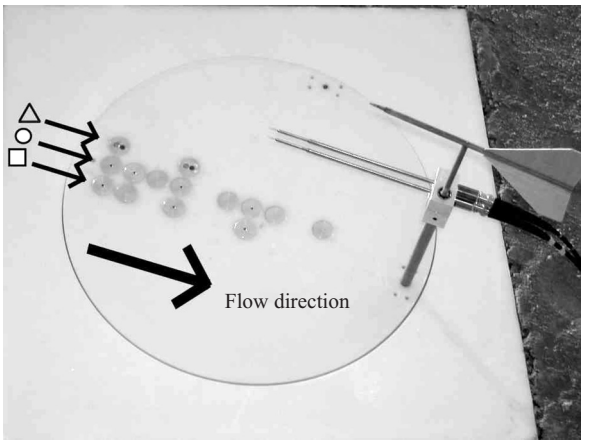

FIGURE 2. Example arrangement of the microphone arrays. △, 23 Hz low-frequency cutoff microphones; ○, 0.07 Hz low-frequency cutoff microphones; □, 1 Hz low-frequency cutoff microphones.

of experimental configurations were realized by rearranging the sensors and using different rotatable plates.

Three different microphones were employed. The experimental configuration shown in figure 2 included two 0.25 in Larson-Davis model 2250 microphones having a frequency response between 23 Hz and 100 kHz, three 0.5 in Larson-Davis model 900B microphones having a frequency response between 1.0 Hz and 100 kHz, and four 0.5 in Bruel and Kjaer model 4193-L-004 microphones having a frequency response between 0.07 Hz and 50 kHz. All of the 0.5 in microphones were fitted with screw-on pinhole caps with 3 mm diameter holes at the top. These were employed to reduce the effective sensing area. The caps were designed to have a Helmholtz resonator frequency exceeding 40 kHz, i.e. well outside the frequency range of the pressure fluctuations associated with the flow over the salt playa.

The signals from the microphones were digitized at a sampling frequency of either 5 kHz or 10 kHz, depending on flow speed. The present data required no additional signal processing as they relate to mitigating the adverse effects of mechanical vibration, electronic or acoustic noise. That is, the only step prior to data reduction involved the conversion of the voltage output from the transducers to Pascals through each transducer's respective linear calibration. This lack of post-processing is not typical since wall-pressure measurements often require the application of noise cancellation and/or filtering to remove extraneous noise (Naguib, Gravante & Wark 1996). Attributes of the current data are exemplified in the computed wall-pressure frequency spectrum of figure 3. Remarkably, the spectrum from the 0.07 Hz microphone produced over seven decades of signal amplitude above the noise floor.

Figure 3 also clearly reveals that the low-frequency cutoff of the transducer significantly affects the capacity to measure the $\sim f^{-1}$ region of the spectrum. Based on estimates of the depth of the atmospheric surface layer, we may surmise that the 0.07 Hz transducers capture the contributions from δ scale eddies. Specifically, typical values for the surface-layer thickness, δ, and the mean velocity at $y = \delta$ are 100 m and 10 m s^{-1}, respectively. Given these values, a δ-sized eddy advecting at U_∞ would generate a frequency of about 0.1 Hz. Comparisons of the present data with the model predictions of Panton & Linebarger (1974) (see § 3.1.2) further support the

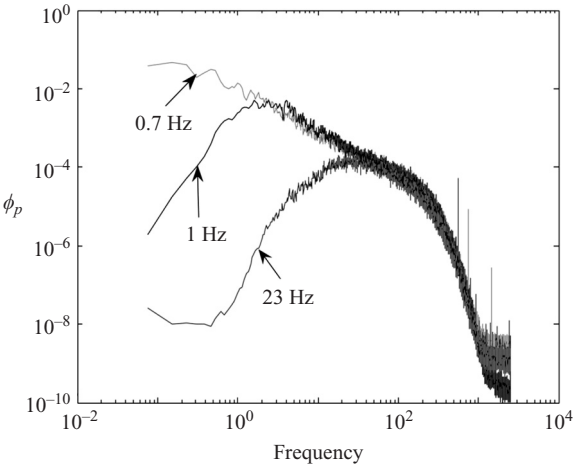

FIGURE 3. Frequency spectra of the surface pressure fluctuations as derived from the different microphones. The indicated frequency refers to the low-end frequency limit inherent to the microphone.

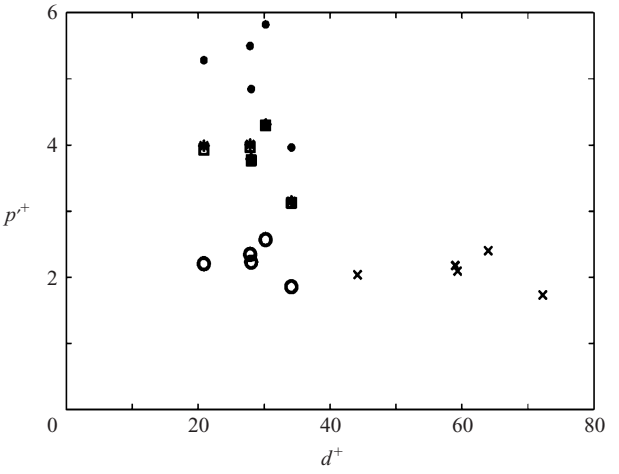

FIGURE 4. Inner normalized wall-pressure intensities as a function of d^+ ●, 0.07 Hz transducer; □ and O, 0.07 Hz transducer high-pass filtered at 1.0 Hz, and 23 Hz respectively; ∗, 1.0 Hz transducer; ×, 23 Hz transducer. Note that the spread of the d^+ values associated with the 0.07 Hz and 1.0 Hz pinhole sensors is representative of the d^+ range associated with the entirety of $p(t)$ time series employed in the analyses of § 3.

conclusion that the present measurements capture a range of frequencies extending from the high-end to below the peak. The effect of the low-frequency cutoff of the microphones relative to the capacity to capture the full spectrum is clearly shown in figures 3 and 4. The point in the spectrum where the low-end attenuation becomes noticeable corresponds closely to the microphone cutoff frequencies of 1 Hz and 23 Hz, respectively. No relative attenuation at the high-frequency end of the spectrum is apparent, even though the 23 Hz transducers had a sensing diameter over twice that of the pinhole microphones.

Figure 4 shows the anticipated decrease in pressure intensity as the low-frequency cutoff of the transducer increases. The data in this plot were simultaneously acquired

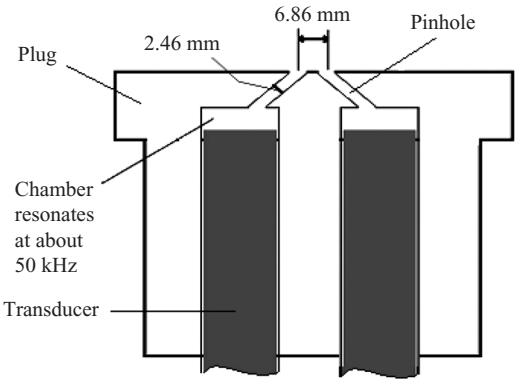

FIGURE 5. Side-view schematic of the surface plug used to determine the in-plane pressure gradients. Shown is a diametrical slice through two of the four pinhole microphones arranged in a square pattern.

from the three different microphones for a series of runs. The 0.07 Hz transducer intensities are seen to be about 1.4 times greater than those derived from the 1.0 Hz microphones. The combination of microphones and pinhole arrangements employed allowed issues relating to spatial and temporal resolution to be further explored. Toward this aim, 1 Hz and 23 Hz high-pass filters were applied to the 0.07 Hz transducer data. This allowed the sensing capabilities of the 1 Hz and 23 Hz transducers to be mimicked. As indicated, the data filtered at 1 Hz nearly identically reproduce the results from the 1 Hz pinhole microphones. High-pass filtering at 23 Hz resulted in even further signficant attenuation in p'^{+}, greater than 40 % relative to the data filtered at 1 Hz. Owing, however, to the pinhole arrangement employed, the data filtered at 23 Hz have a corresponding d^{+} $(=du_{\tau}/\nu)$ that is smaller than that of the 23 Hz microphones. The data of figure 4 indicate only a slight $(\approx 2\,\%)$ attenuation in p'^{+} with increasing d^{+} for the range of d^{+} explored. This result at large δ^{+} differs from the low δ^{+} findings of Schewe (1983) indicating considerable attenuation in the measured wall-pressure intensity for $19 \leqslant d^{+} \leqslant 80$. One possible explanation for this is the fact that, unlike velocity or vorticity, the pressure fluctuations at a point result from a weighted spatial integral. Thus, the present observations may reflect that the vast majority of contributions to this integral in the SLTEST site boundary layer are at scales much larger than the largest d^{+} represented in figure 4 $(d^{+} \approx 73)$. This, of course, is not the case for the same d^{+} in low δ^{+} flows.

2.3.2. *Resolving the wall pressure gradients*

Estimates of the fluctuating wall-pressure gradients were derived in a manner similar to that employed by Andreopoulos & Agui (1996) by finite-differencing the pressure fluctuations simultaneously measured at four closely spaced points in the plane of the surface. The wall-plug shown schematically in figure 5 was employed. Pressure differentials associated with estimating $\partial p/\partial x$ and $\partial p/\partial z$ were taken over the pinhole separation distance of 6.86 mm.

It is well-established that turbulence measurements are susceptible to probe resolution effects (e.g. Johansson & Alfredsson 1983). Gradient measurements are further challenged by their concentration of spectral intensity at higher wavenumbers (Wyngaard 1969; Klewicki & Falco 1990). Consistent with this, Andreopoulos &

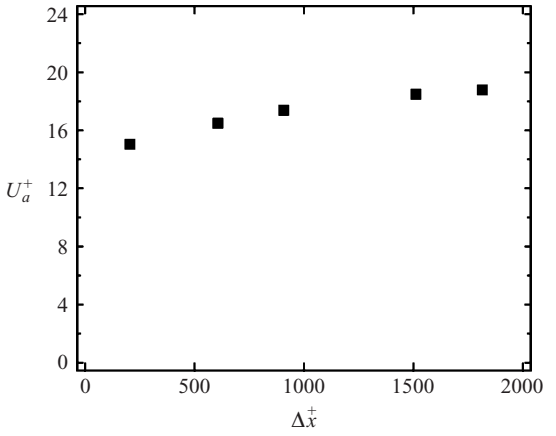

FIGURE 6. Broadband advection velocities computed as a function of the sensor separation.

Agui (1996) found that at $\delta^+ = 2075$, increasing the sensor spacing, Δx^+, from 42 to 59 resulted in attenuation of the measured $(\partial p/\partial x)_{rms}$ by about 25 %.

Gradients were directly estimated by differencing the signals from a pair of the 0.07 Hz pinhole transducers for varying separation distance, and from pairs of the 0.07 Hz, 1 Hz and 23 Hz transducers at their minimum separation distances (6.86 mm, 6.86 mm and 8.3 mm, respectively). Estimates of $\partial p/\partial x$ were also obtained through the use of Taylor's hypothesis. Consistent with the findings of Andreopoulos & Agui (1996), the sensitivity of measuring $\partial p/\partial z$ to sensor resolution was found to be very similar to that for $\partial p/\partial x$.

The sensitivity of the estimated fluctuating pressure gradients to sensor spatial separation could not be directly assessed for separation distances smaller than the minimum, 6.86 mm. Instead, effectively smaller separation distances were explored indirectly through the use of Taylor's hypothesis,

$$\frac{\partial p}{\partial x} \simeq -\frac{1}{U_a}\frac{\partial p}{\partial t}. \tag{2.2}$$

In this equation, U_a is the advection (propogation) velocity associated with the wall-pressure-producing motions. Herein a single value of $U_a^+ = 19$ was employed. This broadband estimate was derived from time-delayed spatial correlations. Specifically, the microphone arrays could be distributed over the range of spatial separations permitted by the size of the mounting plate (see figure 2). Axially aligning the array allowed the construction of space–time correlations, $R_{pp}(\Delta x, \Delta t)$. U_a^+ was calculated by determining the first peak in the correlation between pairs of transducers separated by a distance Δx^+ and the simple relation $U_a^+ = \Delta x^+/\Delta t^+$. The results of these calculations are shown as a function of sensor separation in figure 6. These reveal an increasing trend in U_a with increasing Δx^+ that is consistent with numerous previous studies (e.g. Willmarth & Wooldridge 1962; Bull 1967; Blake 1970). For the largest Δx^+ examined, the measured U_a^+ was 18.8. This is significantly larger than the $U_a^+ \simeq 12$ value reported in previous low-Reynolds-number studies (e.g. Schewe 1983; Choi & Moin 1990). When viewed relative to U_∞, however, it is estimated to be $U_a/U_\infty \simeq 0.5$, which is close to the value of 0.53 cited by Schewe (1983) for high-amplitude events and within the range of $0.4 \lesssim U_a/U_\infty \lesssim 0.8$ given by Snarski & Lueptow (1995). It is, however, smaller than the commonly cited $U_a/U_\infty \simeq 0.8$, for smooth walls (e.g. Willmarth & Wooldridge 1962), or the value of $U_a/U_\infty \simeq 0.73$

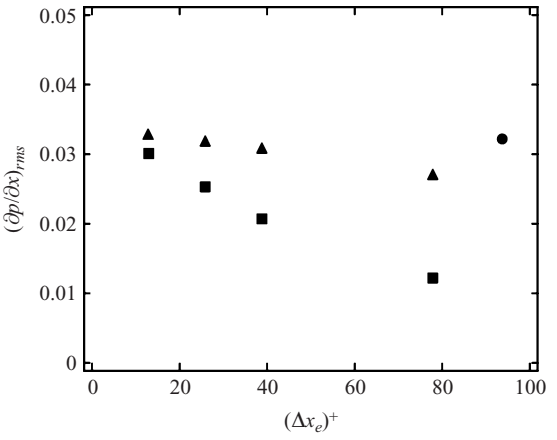

FIGURE 7. Attenuation in $(\partial p/\partial x)_{rms}$ as a function of the effective Δx^+ associated with the use of Taylor's hypothesis. ●, directly estimated spatial derivative ($\Delta x^+ = 93$); ■, Taylor's hypothesis method using a sliding polynomial; ▲, Taylor's hypothesis method using a finite difference.

found by Blake (1970) for rough-wall flows. Since the data of figure 6 are likely to continue to increase for increasing Δx^+, the value of 19 employed herein is believed to be a reasonable lower bound for U_a^+.

Two different methods were used to estimate $\partial p/\partial t$ from the $p(t)$ time series, (*i*) a five-point central difference, and (*ii*) differentiation of a sliding five-point second-order curve fit of the time series. Different values of Δx were then explored (approximately) by successively removing data from the time series at regular intervals. Examination of time series (not shown) reveals that the Taylor-hypothesis-based signal contains about the same high-frequency content and mimics the major features of the spatial-difference-based estimate. With successive point removal, however, both the finite-difference- and curve-fit-based time series lose high-frequency content. This is reflected in figure 7, where the estimates for $(\partial p/\partial x)_{rms}$ consistently attenuate with increasing effective Δx^+, Δx_e^+. For the smallest Δx_e^+ accessible, the finite-difference- and curve-fit-based methods yield nearly the same result, and with increasing Δx_e^+, the curve-fit method has a significantly greater smoothing effect than the finite-difference method. This is because the curve fit is not forced to pass through each data point, and thus with increasing point removal, the peak-to-peak variations in the signal are significantly attenuated.

Also note that the Taylor-hypothesis-based estimates for the minimum Δx_e^+ are in good agreement ($\pm 3\,\%$) with the direct spatial derivative estimate associated with an actual Δx^+ of about 93. A hypothesized explanation for this finds plausibility by noting three observations: (*i*) surface pressure intensity measurements in the present high δ^+ flow are largely insensitive to d^+ for $d^+ \lesssim 75$; (*ii*) the attenuation of $(\partial p/\partial x)_{rms}$ in figure 7 with increasing Δx_e^+ is relatively small for the finite-difference method; and (*iii*) the peak contribution from the $\partial p/\partial x$ power spectrum to $(\partial p/\partial x)_{rms}$ occurs at $f^+ \simeq 0.08$ (see figure 18). The first of these leads to the expectation that the variation in the pressure over a spatial increment of about 90 viscous units will be small at the present δ^+, and thus it is reasonable to expect that derivatives taken over such an increment will provide a good approximation as well. The second observation supports this in that the attenuation is relatively small. Indeed, it is likely that a good portion of this attenuation can be attributed to the inadequacy of the Taylor's hypothesis

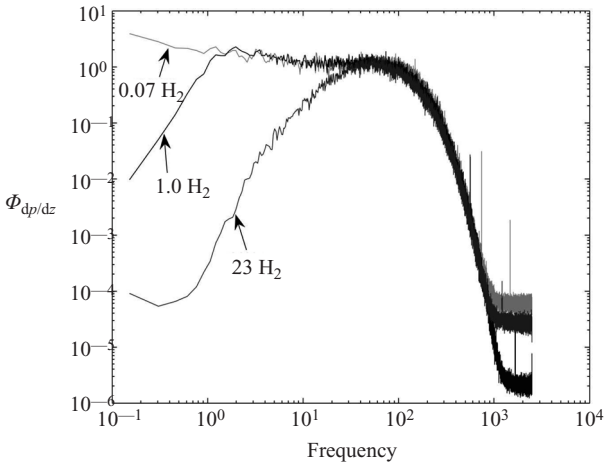

FIGURE 8. Frequency spectra of $\partial p/\partial z$ as derived from pairs of the three different microphones.

approximation using a single advection velocity. Lastly, the third observation reveals that the spectral peak occurs at an estimated advected streamwise length of about 285 viscous units. Thus, given the conservative nature of this estimate (owing to the lower bound value of U_a employed), we can reasonably expect a spatial separation of $\Delta x^+ \approx 90$ to capture most of the derivative intensity.

Figure 8 shows power spectra of $\partial p/\partial z$ as simultaneously derived from pairs of the 0.07 Hz, 1.0 Hz and 23 Hz microphones. For the particular data run shown, the dimensional sensor scales correspond to $\Delta z^+ = 81$, 81 and 98, respectively. As can be seen, the variation in Δz^+ did not result in any detectable attentuation at the high-frequency end of the spectrum, although it is apparent that the noise floor varies from one transducer pair to the next. Because the pressure gradient signal has much more of its spectral intensity concentrated at higher frequencies than does the pressure, the inability to resolve the low frequencies indicated in figure 8 has a less dramatic effect. Comparison of $(\partial p/\partial z)_{rms}$ computed using the 1.0 Hz and 23 Hz microphone pairs with the 0.07 Hz microphone pair reveals attenuations of about 4.5 % and 17 %, respectively.

3. Results

Results are organized relative to the statistics, correlations and spectral features associated with the fluctuating wall pressure. This is followed by a similar presentation relative to the fluctuating surface pressure gradients.

3.1. *Pressure statistics and spectra*

3.1.1. *Wall pressure statistics*

Numerous studies have explored the behaviour of the wall-pressure fluctuations. Well-resolved wall-pressure measurements at $\delta^+ = O(10^6)$ have not, however, been previously reported.

Figure 9 compares the present wall-pressure intensity data at $8 \times 10^5 \lesssim \delta^+ \lesssim 1.2 \times 10^6$ with data from previous low-Reynolds-number experiments. The single data point from the present study represents the average of the ensemble of the intensity values computed from the individual wall-pressure time series selected for

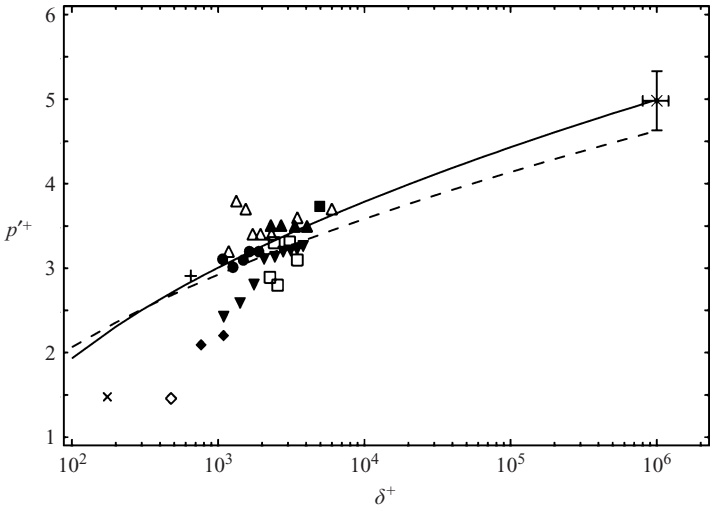

FIGURE 9. Inner normalized wall-pressure intensities as a function of Reynolds number, δ^+. $*$, average of current data, vertical error bars represent $\pm$ one standard deviation of the ensemble of measurements, horizontal error bars represent the estimated δ^+ range; ▼, Tsuji *et al.* (2007); ▲, Blake (1970); ■, Morrison (2007); Morrison *et al.* (1992); △, McGrath & Simpson (1987); ◆, Horne (1989); ●, Farabee & Casarella (1991); □, Bull & Thomas (1976), (open pinhole); +, Schewe (1983); ×, Choi & Moin (1990); ◇, Lauchle & Daniels (1987); —, equation (3.2); – – –, equation (3.1).

analysis. The horizontal and vertical error bars, respectively, represent the approximate Reynolds-number range, and ± 1 standard deviation of the sample scatter about the mean. The mean value is $p'^+ = 4.98$ at $\delta^+ = 1 \times 10^6$. The substantial magnitude change over the δ^+ increment provided by the present experiments supports the conclusion that this increase is statistically significant. Relative to the influence of a transitionally rough wall, the results of Blake (1970) for fully rough flows reveal that p'^+ can vary significantly depending on both the roughness element size and spacing. Given that in the present flow $\delta^+/k_s^+ \gtrsim 10^4$, the vast majority of the sources to the surface pressure come from well outside the roughness sublayer – a condition not necessarily true for the same k_s^+ at lower δ^+.

A number of arguments have been used to predict an increase in p'^+ with increasing δ^+. Bradshaw (1967) used dimensional reasoning and/or the substitution of universal range variables (τ_w and k_1, the streamwise wavenumber) into the Poisson equation for pressure to deduce the existence of an intermediate spectral range where $\Phi(k_1) \sim k_1^{-1}$. This leads to the prediction that the inner normalized wall-pressure variance exihibits a logarithmic dependence on δ^+, $(p'^+)^2 \sim \log(\delta u_\tau/\nu)$. Panton & Linebarger (1974) arrive at the same prediction by formulating a Millikan-type (Millikan 1939) overlap-layer hypothesis for the surface-pressure spectrum. These and similar formulations are consistent with the empirical observation that the (approximate) y and u_τ scaling properties of the logarithmic-like portion of the mean velocity profile correlate with the sources for the surface-pressure fluctuations. Specifically, the inner normalized depth of this scaling layer increases approximately logarithmically with increasing δ^+. Farabee & Casarella (1991) capitalized on this observation to predict the Reynolds-number dependence of p'^+ by numerically integrating estimated pressure spectra over the intermediate wavenumber range corresponding to this layer. This resulted in (3.1), reflecting that the wall pressure

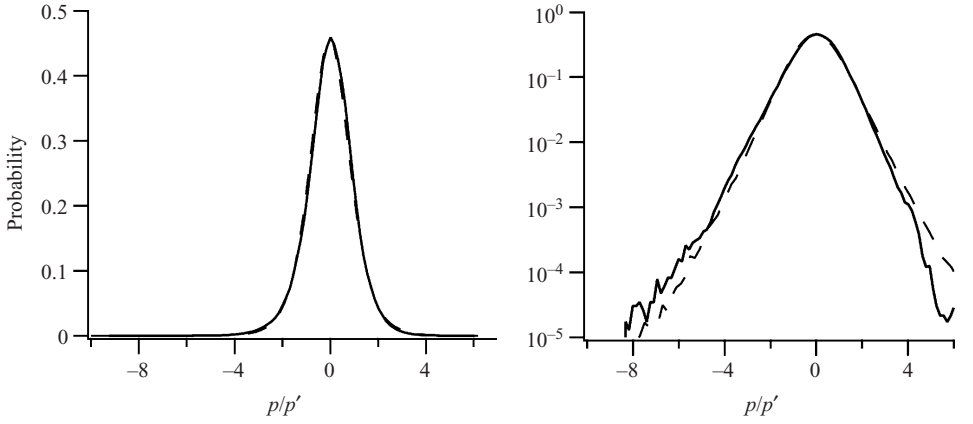

FIGURE 10. Probability density function of the fluctuating wall pressure. —, present; – – –, Tsuji *et al.* (2007), $\delta^+ = 3826$.

variance increases logarithmically with increasing δ^+. The constants in this expression are empirically determined from the relatively low δ^+ data available to Farabee & Casarella (1991). The results of figure 9 reveal that at $\delta^+ = 1 \times 10^6$, the extrapolation of (3.1) differs from the present data point by about one standard deviation of the ensemble of p'^+ measurements. Figure 9 also displays a modified version of (3.1) (equation (3.2)), that has a different multiplicative constant. This equation more accurately captures the Reynolds-number dependence indicated by the present data.

$$\frac{p_{rms}}{\tau_w} = \sqrt{6.5 + 1.86\ln\left(\frac{\delta^+}{333}\right)}, \tag{3.1}$$

$$\frac{p_{rms}}{\tau_w} = \sqrt{6.5 + 2.30\ln\left(\frac{\delta^+}{333}\right)}. \tag{3.2}$$

An example probability density function (p.d.f.) of the fluctuating wall pressure at $\delta^+ \simeq 1 \times 10^6$ is shown in figure 10. The result from Tsuji *et al.* (2007) at $\delta^+ = 3826$ is included for comparison. On linear axes the present p.d.f. is indistinguishable from that of Tsuji *et al.* (2007), while on semi-logarithmic axes some small deviations in the tails of the distributions are evident. The logarithmic representation of the p.d.f. clearly reveals a negatively skewed distribution. Results from previous low-Reynolds-number experiments most prevalently indicate that $S(p) = -0.05$ to -0.2 (e.g. Andreopoulos & Agui 1996; Snarski & Lueptow 1995). Schewe (1983) showed that at $\delta^+ \simeq 600$, measurements with sensors having a d^+ greater that about 50 failed to produce a negative $S(p)$. (Note that because the pressure at a point results from an integral over the half-space, a resolution of $d^+ = 50$ at low Reynolds number captures a significantly smaller fraction of the contributing motions than a $d^+ = 50$ resolution at high Reynolds number.) Schewe further revealed that high-frequency high-amplitude negative events in the $p(t)$ signal underlie the negative skewness. The ensemble mean of the $S(p)$ values derived from the present experiments is -0.11. As shown in figure 4, for the present experiments d^+ fell almost exclusively in the range $15 \leqslant d^+ \leqslant 40$. The ensemble mean of the computed fourth central moments of $p(t)$ is $K(p) = 4.94$. This value is also comparable to low-Reynolds-number results (Schewe 1983; Snarski & Lueptow 1995; Andreopoulos & Agui 1996). The logarithmic plot

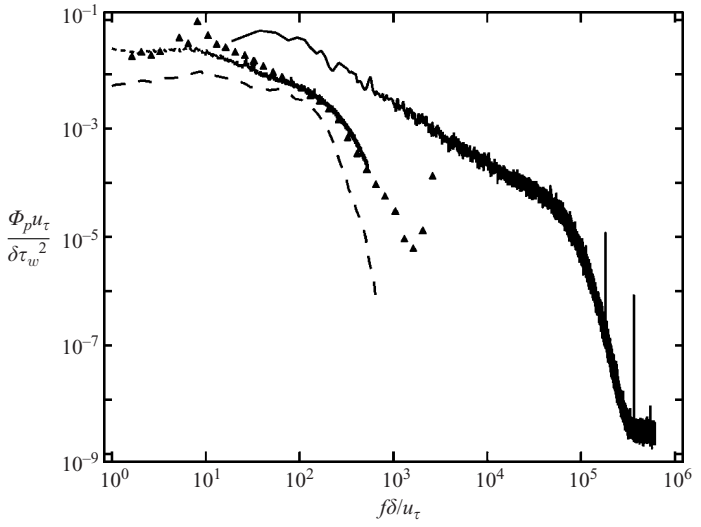

FIGURE 11. Outer normalized frequency spectra of the wall pressure; ——, present data $\delta^+ \simeq 1 \times 10^6$; - - -, Farabee & Casarella (1991) $\delta^+ = 2010$; . . . , Tsuji *et al.* (2007) $\delta^+ = 3822$; ▲, Morrison (2007) $\delta^+ = 4956$.

reveals that the p.d.f. of the surface pressure at high Reynolds number has significantly non-Gaussian tails, and is slightly more negatively skewed than the p.d.f. of Tsuji *et al.* (2007) at $\delta^+ = 3826$.

3.1.2. *Wall pressure spectra and correlations*

Representing experimentally derived frequency spectra in terms of streamwise wavenumber requires an expression for the advection velocity associated with pressure producing motions, $U_a = U_a(k_1)$. Consistent with the concept that the streamise wavenumbers associated with the boundary-layer motions scale inversely with their positions from the wall, most existing data and supporting analyses indicate that U_a approximately follows a negative logarithmic function of frequency (Panton & Linebarger 1974; Panton & Robert 1994). Given that $f = k_1 U_a(k_1)$, it is a simple task to represent frequency spectra from wavenumber spectra. Transforming frequency spectra to wavenumber spectra is not as straightforward. Panton & Linebarger (1974) note, however, if $U_a(k_1)$ is non-constant, the slope of the $\sim k_1^{-1}$ region of the wavenumber spectrum is preserved as an $\sim f^{-1}$ region in the corresponding frequency spectrum.

Panton & Linebarger (1974) also suggest that Reynolds-number effects are minimized by plotting $\Phi_p(f)u_\tau/\tau_w^2\delta$ versus $f\delta/u_\tau$. A representative pressure spectrum from the present experiments is plotted in this manner in figure 11. As indicated, greater than three decades of approximately -1 slope is present. A curve fit of these data over $3.5 \leqslant \log(f\delta/u_\tau) \leqslant 4.5$ yields a value for the slope of -1.04. This value is of higher magnitude than reported in most previous low δ^+ studies (i.e. is closer to a value of -1). The close correspondence to the -1 slope is also clearly reflected in the pre-multiplied spectrum of figure 13.

The data of Farabee & Casarella (1991), Tsuji *et al.* (2007) and Morrison (2007) at $\delta^+ = 2010$, 3822 and 4956, respectively, are also shown in figures 11 and 12. Comparison reveals that under outer normalization, the peak in the spectrum from the low-Reynolds-number studies is situated at about half a decade lower normalized

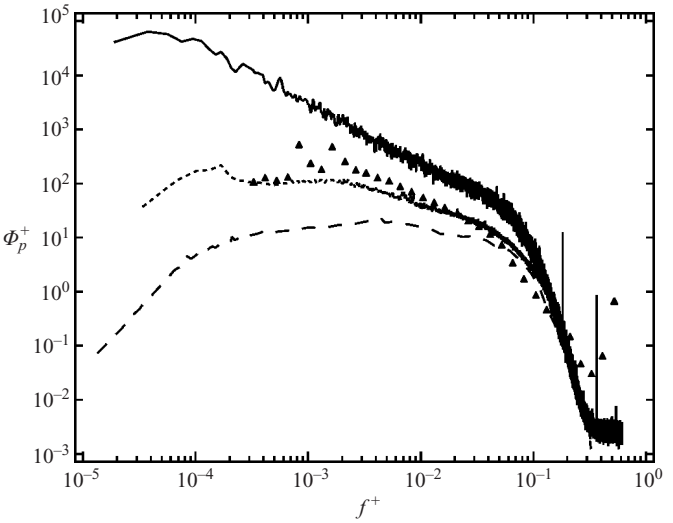

FIGURE 12. Inner normalized frequency spectra of the wall pressure. Symbols as in figure 11.

frequency than the present spectrum. This would seem to indicate that under this normalization the position of the peak exhibits a Reynolds-number dependence. (Note that the peak in the present spectrum occurs at $f > 0.07$ Hz, and thus its position is not an artefact of the transducer cutoff frequency. Note also that the use of $\delta^+ = 8 \times 10^5$ rather than $\delta^+ = 1 \times 10^6$ is insuffucient to account for the observed shift in the peak.) The -1 region also tends to be less apparent in the low-Reynolds-number data. Unlike most studies at low Reynolds number, the spectrum of Morrison (2007) exhibits a slope close to -1. The more typically observed deviation from a -1 slope is apparent in the inner-normalized spectra of Farabee & Casarella (1991) and Tsuji *et al.* (2007). The latter of these exhibits a discernible region of -0.7 slope. Overall, these data suggest that the slope of the constant slope region asymptotes to a value close to -1 as δ^+ becomes large, and that the spectral intensity of the -1 region increases with increasing δ^+. Regarding this last point, it is relevant to note that the p'^+ value associated with the $\delta^+ \simeq 1 \times 10^6$ spectrum shown is 4.95, and thus is representative of the mean of the ensemble of normalized pressure signals acquired. (Recall that the ensemble mean p'^+ value in figure 9 is 4.98.)

The roll-off at high frequency is similar between the high- and low-Reynolds-number spectra. Buffer-layer contributions to the surface pressure have been associated with a -5 slope in the pressure spectrum (e.g. Bradshaw 1967). At high frequencies, the present spectrum transitions from a slope near -1 to something less than -6, and thus there is a relatively small frequency band for which the slope is approximately -5. This frequency band, however, is not distinctly apparent. A curve fit of the present spectrum between $5.1 \leqslant \log(f\delta/u_\tau) \leqslant 5.4$ yields a slope of about -7. As expected, when normalized by inner variables (figure 12) the present spectrum and those measured at lower Reynolds numbers merge at high frequencies.

Overall, the present spectrum shows good qualitative and quantitative agreement with the calculated spectra of Panton & Linebarger (1974). When plotted according to the normalization of figure 11, their calculations predict a peak value close to that shown. Similarly, based upon an extrapolation of their results, we should expect about three decades of $\sim f^{-1}$ behaviour; also in accord with the present data. Their

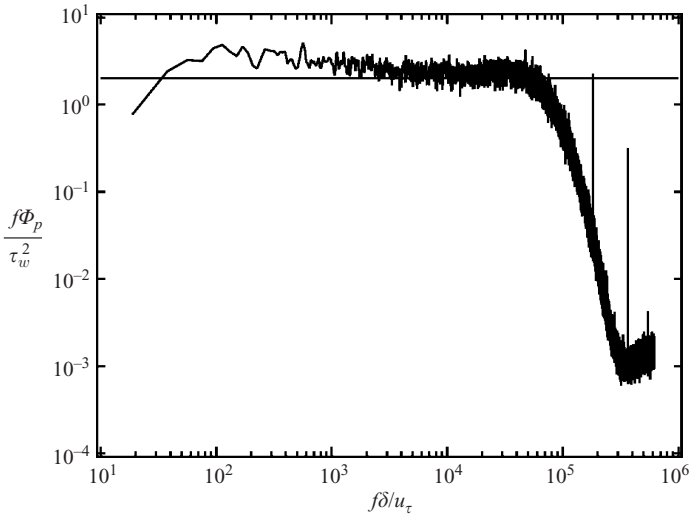

FIGURE 13. Pre-multiplied spectrum of the wall-pressure fluctuations.

model also predicts that the low-frequency end of the spectrum rises above the f^{-1} line. The data of figures 11 and 12 do not readily indicate this behaviour. As figure 13 shows, however, the present data do exhibit this behaviour, but not as distinctly as their model predicts. Possible explanations are that their model calculations are based upon an irrotational and isothermal free stream, whereas the outer region of the atmospheric surface layer is bounded by a turbulent 'free stream', and, even under the near-neutral stability conditions, will contain motions that formed under unstable conditions.

The autocorrelation of the wall-pressure signal, $R_{pp}(\Delta t)$, as derived from a 0.07 Hz pinhole microphone, is shown for a variety of time-delay normalizations in figures 14 and 15. In figure 14, R_{pp} is plotted versus Δt^+ on semilogarithmic axes. One apparent feature of this curve is that the first zero-crossing occurs at a time delay corresponding to about 5000 viscous time scales. If this time is converted to a length, then the corresponding advected length is about 0.1δ. Given that $U_a^+ = 19$ is estimated to be a lower bound, we can conservatively estimate the advected length to be somewhere between 0.1δ and 0.2δ. Another apparent feature of figure 14 is the approximately logarithmic variation of R_{pp} over an extensive range of time delays; $20 \lesssim \Delta t^+ \lesssim 1000$. Relative to the spectrum of figure 11, this approximately corresponds to the -1 spectral region. Similarly, the 'knee' in the curve near $\Delta t^+ = 10$ corresponds to the transition from the high-frequency portion of the spectrum (associated with the buffer layer and below) to that associated with the logarithmic-layer motions. Lastly, it is worth noting that the features exemplified in figure 14 were consistently revealed in all of the R_{pp} examined.

Figure 15 explores alternative normalizations of the R_{pp} time delay. These include $\Delta t u_\tau/\delta$, $\Delta t U_\infty/\delta$ and $\Delta t u_\tau/2\sqrt{\nu\delta/u_\tau} = \Delta t^+/2\sqrt{\delta^+}$. The first of these is the inverse of the outer normalization for frequency employed in figure 11. The second is an outer normalization based upon U_∞ and δ. The third is based upon u_τ and an intermediate length scale, $2\sqrt{\nu\delta/u_\tau}$. This length has been shown empirically to correspond to the position of the peak of the Reynolds stress (Long & Chen 1981; Sreenivasan 1989), and both empirically and analytically shown to be intrinsic to the scaling structure of

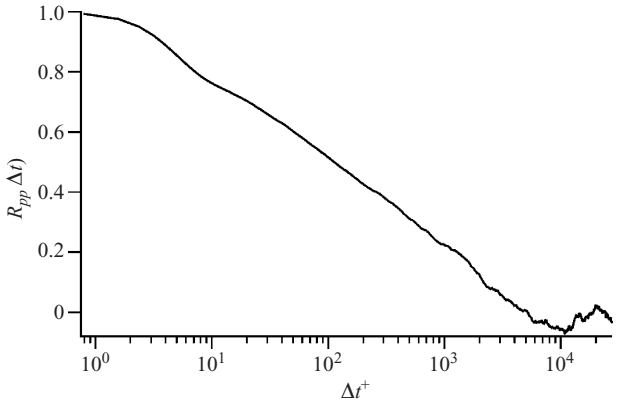

FIGURE 14. Autocorrelation of the wall pressure versus inner-normalized time delay.

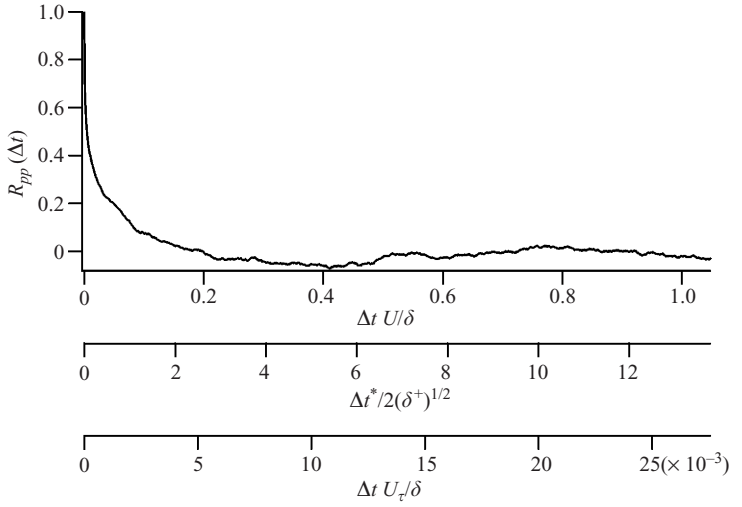

FIGURE 15. Wall pressure autocorrelation versus outer- and meso-normalized time delay.

the mean momentum balance (Wei *et al.* 2005). Relative to wall pressure, Bradshaw (1967) draws a connection between this length scale and the centroid of the k_1^{-1} region of the wall-pressure spectrum. The position of the first zero-crossing occurs at a non-dimensional time delay of about 5×10^{-3} for the $\Delta t u_\tau/\delta$ normalization. In contrast, the zero-crossing occurs near 0.2 and 2.5, respectively, for the $\Delta t U_\infty/\delta$ and $\Delta t u_\tau/2\sqrt{\nu\delta/u_\tau}$ normalizations. Both of these normalizations are consistent with the notion that the most appropriate normalization would place the zero crossing at an $O(1)$ non-dimensional time delay. Thus, the former suggests that the time to the first zero-crossing has association with advecting $O(\delta)$ eddies, whereas the latter suggests a connection with pressure sources characteristic of the k_1^{-1} portion of the spectrum.

3.2. *Pressure gradient statistics and spectra*

3.2.1. *Pressure gradient statistics*

The predominant sources of time-resolved vorticity flux data are the relatively low δ^+ studies of Andreopoulos & Agui (1996) and Honkan & Andreopoulos (1997). A

Study	δ^+	$\frac{\nu^2}{u_\tau^3}$	$\frac{\nu}{u_\tau U_\infty}\sqrt{\frac{\nu\delta}{u_\tau}}$	$\frac{\theta^2}{u_\tau}$	$\frac{\nu^2}{U_\infty u_\tau^2}$	$\sqrt{\frac{\nu^2\delta^2}{U_\infty u_\tau^3}}$	$W^+\left(\frac{\partial\omega_x}{\partial y}\right)^+_{rms}$	$\frac{W^+}{p'^+}\left(\frac{\partial p}{\partial z}\right)^+_{rms}$
AA96	1315	0.063	0.094	1063	0.0026	16.80	4.22	1.36
AA96	1472	0.058	0.090	1228	0.0024	17.09	3.97	1.26
AA96	1575	0.048	0.076	1168	0.0019	14.89	3.33	1.05
AA96	1750	0.035	0.058	1047	0.0014	12.19	2.47	0.76
AA96	1910	0.030	0.052	1069	0.0012	11.33	2.15	0.66
AA96	2075	0.021	0.037	928	0.0008	8.59	1.53	0.47
Present	1×10^6	0.038	1.06	20.4×10^6	0.001	1925	5.21	1.04

TABLE 1. Non-dimensional values of $(\partial\omega_x/\partial y)_{rms}$ according to various normalizations. In the last two columns, the data are made non-dimensional using $\nu W/u_\tau^2$ and W/p', where W^+ is the inner normalized pocket width as given by (4.1), and the inner normalized wall-pressure intensities were computed using (3.2). The data are from the present study and Andreopoulos & Agui (1996).

primary objective of the present analysis is to use the vastly larger δ^+ condition to advantage in clarifying the scaling behaviour of vorticity flux intensities. Toward this aim, a number of normalizations were explored by comparing our present results with those of Andreopoulos & Agui (1996).

Vorticity gradients have the dimensions of frequency per length, and thus are made non-dimensional via multiplication with a length squared over velocity. Given this, combinations of candidate length and velocity scales were investigated. The characteristic lengths considered were ν/u_τ, $\sqrt{\nu\delta/u_\tau}$, δ and θ (the momentum deficit thickness). The characteristic velocities considered were u_τ and U_∞. Table 1 presents the non-dimensional values of $(\partial\omega_x/\partial y)_{wall}$ according to normalizations that use a variety of combinations of these characteristic length and velocity scales. In general, the normalizations sought are those that produce non-dimensional values that are fixed for all Reynolds numbers and have an $O(1)$ magnitude. In connection with the $(\partial\omega_x/\partial y)_{rms}$ data of table 1, it is relevant to note that the normalized values of $(\partial\omega_z/\partial y)_{rms}$ exhibit nearly identical behaviours.

When subjected to normalization by the two combinations of mixed variables explored, $\nu/(u_\tau U_\infty)\sqrt{\nu\delta/u_\tau}$ and $\sqrt{\nu^2\delta^2/U_\infty u_\tau^3}$, the high- and low-Reynolds-number data of table 1 exhibit a variation of about two orders of magnitude. Similarly, the high-Reynolds-number data, when normalized by θ^2/u_τ, attains a value that is about four orders of magnitude larger than the similarly normalized low δ^+ data. Per the analysis of Andreopoulos & Agui (1996) (and as reflected in table 1), this normalization essentially removes Reynolds-number dependence over the relatively low δ^+ range of their study. In contrast, both the purely viscous normalization, ν^2/u_τ^3, and the normalization, $\nu^2/(U_\infty u_\tau^2)$, result in values that are the same order of magnitude at both high and low-Reynolds-number. As indicated by the tabulated data and in the graphical representation of the viscous normalization in figure 16, under these normalizations the low-Reynolds-number data still vary by a factor of about three. One possible explanation for these observations is that under these or other similar normalizations, the vorticity flux intensities undergo a rapid variation at low Reynolds number and then attain an essentially constant value as δ^+ becomes large. Well-resolved data at $\delta^+ = O(10^5)$ would go far in clarifying this issue. It is additionally worth noting that none of the normalizations that use combinations of

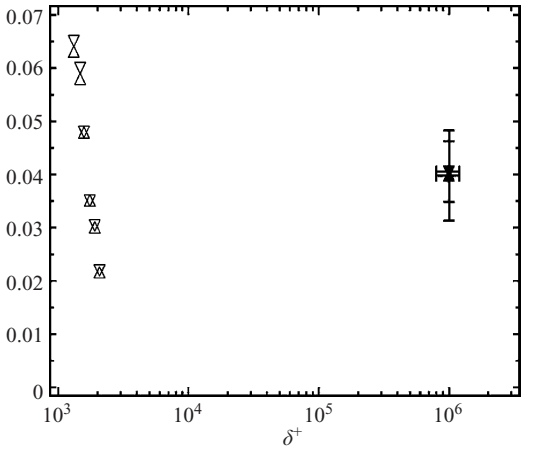

FIGURE 16. Inner normalized surface vorticity flux intensities versus Reynolds number, δ^+. ▲, average of the present $(\partial\omega_x^+/\partial y^+)_{rms}$ data, vertical error bar represents $\pm$ one standard deviation of the data scatter; ▼, average of present $(\partial\omega_z^+/\partial y^+)_{rms}$ data, vertical error bar represents $\pm$ one standard deviation of the data scatter, △, $(\partial\omega_x^+/\partial y^+)_{rms}$ data of Andreopoulos & Agui (1996); ▽, $(\partial\omega_z^+/\partial y^+)_{rms}$ data of Andreopoulos & Agui (1996).

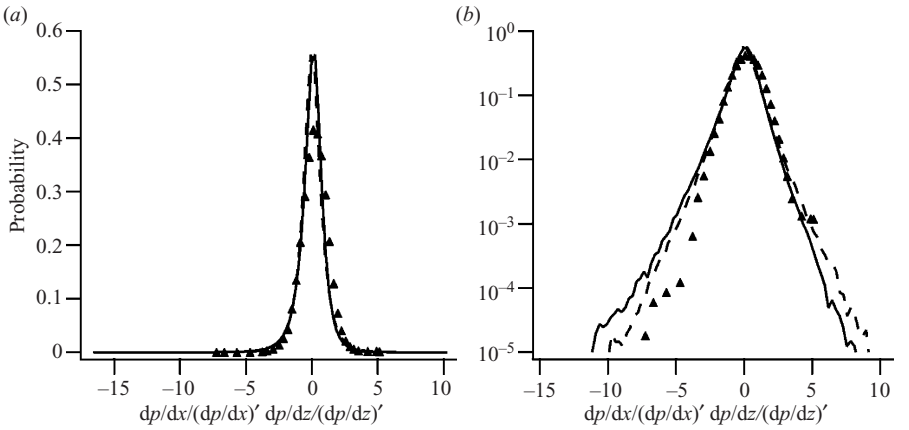

FIGURE 17. —, Probability density functions of the streamwise wall-pressure gradient fluctuations; and ----, spanwise wall-pressure gradient fluctuations; ▲, streamwise wall-pressure gradient fluctuation p.d.f. of Andreopoulos & Agui (1996).

the aforementioned length and velocity scales yield non-dimensional values that are $O(1)$ independent of δ^+.

The probability density functions of the fluctuating wall-pressure gradients (surface vorticity fluxes) shown in figure 17 are highly non-Gaussian. When plotted on linear axes, the p.d.f.s of $(\partial p/\partial x)_{wall}$ and $(\partial p/\partial z)_{wall}$ are shown to be similar, each exhibiting a relatively sharp peak about zero and long low-amplitude tails. These features are consistent with the large kurtosis values of 8.6 and 8.0 for $(\partial p/\partial x)_{wall}$ and $(\partial p/\partial z)_{wall}$, respectively. The logarithmic plot reinforces that the tails of the p.d.f.s are non-Gaussian, and more clearly reveals that the $(\partial p/\partial x)_{wall}$ p.d.f. is negatively skewed whereas the $(\partial p/\partial z)_{wall}$ p.d.f. exhibits a high degree of symmetry. These observations are reflected in the measured skewness values of -0.7 and 0 for $(\partial p/\partial x)_{wall}$ and

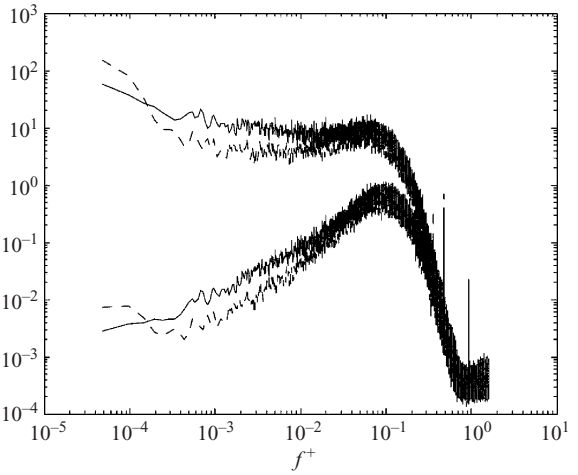

FIGURE 18. —, Inner normalized spectra (upper curves) and inner normalized pre-multiplied spectra (lower curves) of the streamwise wall pressure gradient fluctuations, and - - - -, spanwise wall pressure gradient fluctuations.

$(\partial p/\partial z)_{wall}$, respectively. The skewness of the $(\partial p/\partial z)_{wall}$ p.d.f. is expected to be zero in a two-dimensional mean flow. The negative skewness associated with $(\partial p/\partial x)_{wall}$ indicates that high-amplitude events tend to favour the production of spanwise vorticity having the same sign as the mean. For comparison, figure 17 also presents the $(\partial p/\partial x)_{wall}$ p.d.f. data of Andreopoulos & Agui (1996), which is similar to their $(\partial p/\partial z)_{wall}$ p.d.f. This p.d.f. exhibits a significantly lower peak value than the present, is more broadly distributed around the peak, and is not appreciably skewed. Consistent with these observations, Andreopoulos & Agui (1996) report skewness values of about 0 and -0.1 for $(\partial p/\partial z)_{wall}$ and $(\partial p/\partial x)_{wall}$, respectively and kurtosis values between 3.6 and 4.2 for $1315 \leqslant \delta^+ \leqslant 2075$.

3.2.2. *Pressure gradient spectra and correlations*

Inner normalized spectra and pre-multiplied spectra of the wall-pressure gradient fluctuations are presented in figure 18. As indicated, the $(\partial p/\partial x)_{wall}$ and $(\partial p/\partial z)_{wall}$ spectra are quite similar. The surface pressure gradient spectra reported by Andreopoulos & Agui (1996) (not shown) are somewhat different. Specifically, their results indicate that for frequencies below about $f^+ = 0.1$ both the $(\partial p/\partial x)_{wall}$ and $(\partial p/\partial z)_{wall}$ spectra exhibit a nearly constant negative slope. When θ and u_τ are employed they show that the variation of their spectra is approximated by an $(f\theta/u_\tau)^{-0.75}$ dependence. The data in table 1 indicate that this normalization does not account for Reynolds-number dependence when the present data are included. Furthermore, while both the present $(\partial p/\partial x)_{wall}$ and $(\partial p/\partial z)_{wall}$ spectra show upward trendencies at low frequencies, it is deemed unduly speculative to attach a slope to this trend (i.e. a reasonable estimate is that these spectra are approximately flat for a range of frequencies, $f^+ < 0.1$).

The pre-multiplied spectra of figure 18 reveal a peak near $f^+ = 0.08$. Furthermore, the drop-off from this peak at both higher and lower frequencies is considerable. Given that the area under pre-multiplied spectrum can be approximately interpreted as a graphical depiction of the weighted (per frequency increment) contributions to the signal variance, the results of figure 18 reveal that even at this high Reynolds number

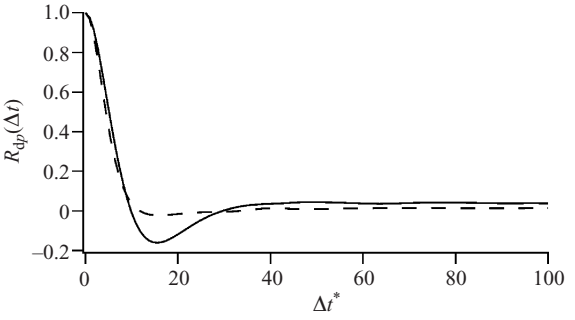

FIGURE 19. Autocorrelations of the fluctuating wall-pressure gradients, —, streamwise pressure gradient; - - - -, spanwise pressure gradient.

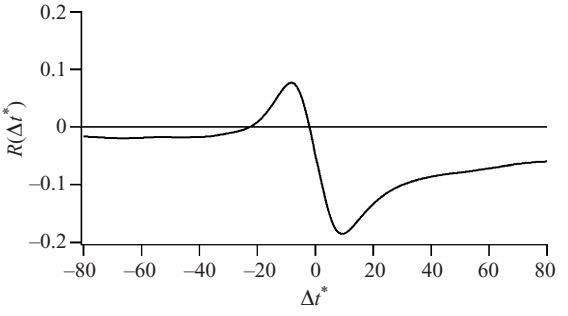

FIGURE 20. Temporal correlation between the fluctuating streamwise wall pressure gradient and the wall pressure.

the motions involved in the surface flux of vorticity are confined to a relatively narrow band of dynamically significant scales. The frequency associated with this peak corresponds to an advected length of $x^+ \simeq 285$.

A number of statistical measures associated with the pressure and pressure gradients were examined. Two of these are shown in figures 19 and 20. Others that are not shown include the joint p.d.f. of $\partial p/\partial x$ and $\partial p/\partial z$, and the cross-correlation between $\partial p/\partial x$ and $\partial p/\partial z$ as a function of time delay. Like the result of Andreopoulos & Agui (1996), the joint p.d.f. of $\partial p/\partial x$ and $\partial p/\partial z$ exhibits essentially circular contours. Similarly, the normalized time-delayed correlation of $\partial p/\partial x$ and $\partial p/\partial z$ essentially displays a unity spike at $\Delta t^+ = 0$ and is otherwise zero. These findings indicate the absence of a preferential statistical structure between $\partial p/\partial x$ and $\partial p/\partial z$. Both of these results are likely to be tied to the fact that the z-direction is one for which the flow properties are statistically homogeneous.

Figure 19 shows the autocorrelations of $\partial p/\partial x$ and $\partial p/\partial z$ as a function of inner-normalized time delay. For $\Delta t^+ \lesssim 10$ both of the curves in figure 19 are nearly identical strongly decreasing positive functions. For greater time delays, the autocorrelation of $\partial p/\partial z$ remains essentially zero, whereas the autocorrelation of $\partial p/\partial x$ exhibits a distinctive negative peak at $\Delta t^+ \simeq 15$. The advected length associated with this time delay is $\Delta x^+ \simeq 285$, and thus is the same as that associated with the peak in the pre-multiplied spectra of figure 18.

Further clarification regarding the negative peak in the $\partial p/\partial x$ autocorrelation is revealed in figure 20. This figure shows the normalized time-delayed correlation

between the $\partial p/\partial x$ fluctuations and p itself. The resulting signature is characterized by a relatively low-amplitude positive peak for negative time delays, followed by a higher-amplitude negative peak for positive Δt^+. For larger time delays (both negative and especially positive) the correlation exhibits lower-level negative values. The rise toward zero for $\Delta t^+ > 0$ is quite slow, taking hundreds of viscous time scales (not shown). In accord with the $\partial p/\partial x$ autocorrelation of figure 19, the time delay between the positive and negative peaks is about 15 viscous time scales. From these results, we can surmise that the underlying flow process is characterized by an advecting and spatially localized pressure perturbation. In the case of a positive pressure fluctuation, $\partial p/\partial x$ will be positive for negative times (upstream) and become negative when the positive p perturbation begins to attenuate back toward zero. In the case of a negative pressure fluctuation, the sign of the corresponding $\partial p/\partial x$ signal is reversed. The low-level negative correlation suggests that the localized pertubation is embedded in a larger-scale pressure event that is tending toward $p = 0$; i.e. p is either a decreasing positive value or an increasing negative value.

4. Discussion and conclusions

Measurements of the fluctuating wall pressure and its in-plane gradients were made in the high-Reynolds-number turbulent boundary layer that exists over the salt playa of western Utah, USA. The requirements for good resolution measurements were clarified and the present pressure and pressure gradient measurements were demonstrated to be well resolved. Many of the results relating to the pressure fluctuations could be connected to low-Reynolds-number trends. Conversely, while a number of normalizations for the surface vorticity flux intensities were explored, and some were found to produce non-dimensional values that retained the same order of magnitude over the $10^3 \leqslant \delta^+ \leqslant 10^6$ range, none produced values that were either $O(1)$ or that convincingly connected the present results to existing low δ^+ trends.

The fact that $(\partial p/\partial x)_{rms} \simeq (\partial p/\partial z)_{rms}$ is consistent with the lower δ^+ results of Emmerling (1973), indicating that surface-pressure perturbations initiate with a nearly circular shape. Falco (1983, 1991) associates these perturbations with sublayer pockets. In this context, it is relevant to note that the scale of the average inner-normalized width of pockets, W, exhibits a logarithmic dependence on Reynolds number over the range $1 \times 10^3 \lesssim R_\theta \lesssim 2 \times 10^6$ (Klewicki *et al.* 1995; Fershtut 2006; Metzger *et al.* 2007*b*),

$$W^+ = -17.5 + 24.2 \log(R_\theta). \tag{4.1}$$

This increase in scale with increasing δ^+ is consonant with the present results indicating that the surface-pressure gradient fluctuations at high Reynolds number can be accurately estimated with larger inner normalized transducer separations than at low δ^+. Furthermore, at $\delta^+ = 1 \times 10^6$ ($R_\theta \simeq 2.5 \times 10^6$), (4.1) gives $W^+ = 137.3$. The typical pocket length, L, is about twice its width (Falco 1991), $L^+ \simeq 275$, and thus is remarkably close to the characteristic scale associated with the present pressure gradient fluctuations. These observations foster consideration of the following heuristic scaling arguments for the pressure gradient intensities.

Existing evidence is that pocket formation is connected to some family of vortical motions that come in proximity to the wall (e.g. Falco 1991; Smith *et al.* 1991). Primary factors associated with the resulting scale and intensity of the surface-pressure gradient perturbations are reasoned to include the characteristic vortical

intensity of the initiating motion, its advective speed and angle with the wall. As a first approximation, we hypothesize that the pressure gradient intensities scale with a characteristic vorticity magnitude and a characteristic length. High-Reynolds-number data indicate that both the spanwise and wall-normal vorticity component intensities scale with wall variables (Priyadarshana *et al.* 2007), justifying use of u_τ^2/ν as a characteristic vorticity scale. The pocket width, W, is employed as the characteristic length. The resulting normalized values are given in the eighth column of table 1. Under this normalization, the previously noted inconsistency between the low δ^+ data trend and the high δ^+ data point persists, although the relative variation of the low δ^+ data is slightly reduced. Unlike inner normalization, however, use of W and u_τ^2 results in $O(1)$ values at all δ^+. Clearly, scaling the characteristic vortical motion source contributions to the wall pressure gradient intensities involves a more complicated δ^+ dependence than inner normalizaton alone. This point is reflected by the fact that p'^+ itself exhibits an unambiguous increase with δ^+ (figure 9), and is reinforced by considering a normalization that directly incorporates a characteristic pressure and length scale. The last column of table 1 reveals that normalization by W and p' yields a slightly smaller relative variation of the low δ^+ data, but clearly does not remove the rapidly decreasing trend. All the data are $O(1)$ under this normalization, and at $\delta^+ = 1 \times 10^6$ it yields a non-dimensional value very close to 1.0. Overall, these heuristic analyses suggest that the Reynolds-number dependence of the characteristic length scale associated with the surfac-pressure gradient fluctuations is captured by the Reynold-number dependence associated with the sublayer pocket motions. The complete scaling of the gradient intensities, however, remains unclear.

Lastly, it is relevant to note that the wall gradient fluctuations of spanwise vorticity in the present high-Reynolds-number flow are characterized by a rapid transition between opposing sign extremes. This observation is in accord with the previous low δ^+ observations of Andreopoulos & Agui (1996), although the inner normalized scale of these rapid transitions increases with Reynolds number. Relative to the overall structure of the turbulent boundary layer, this represents a generic (essentially unavoidable) mechanism by which spatially compact motions bearing opposing sign vorticity are introduced into the flow. There is an enormous and ever-increasing body of evidence that counter-rotating vortical motions factor significantly in the transport mechanisms of the boundary layer, e.g. see the numerous references in Robinson (1991) as well as Falco (1991); Klewicki *et al.* (1990); Klewicki (1997); Klewicki & Hill (1998); Klewicki & Hirschi (2004); Wu & Christensen (2006); Natrajan *et al.* (2007). Furthermore, given that a primary mechanism for pocket initiation is associated with the presence of positive $\tilde{\omega}_z$ close to the wall (note that the sign of the mean vorticity is negative in the present coordinate system) (e.g. Falco 1991), this *bipolar* generation of spanwise vorticity is also likely to be highly correlated with its own continual regeneration. Such considerations naturally lead to the hypothesis that the specific mixture and scale of positive and negative vorticity fluctuations is an irreducible attribute of boundary-layer turbulence.

The authors are pleased to acknowledge the contributions of Brendan Perkins, David Kenney, Heidi Miner and Rachel Packard. We also thank Professors Jonathan Morrison and Yoshiyuki Tsuji for providing their data. This work was supported by the National Science Foundation under grants CTS-0120061 and CBET-0555223 (grant monitors, M. Plesniak and W. Schultz) and the Office of Naval Research under grant N00014-00-1-0753 (grant monitor, R. Joslin).

REFERENCES

Andreopoulos, J. & Agui, J. H. 1996 Wall-vorticity flux dynamics in a two-dimensional turbulent boundary layer. *J. Fluid Mech.* **309**, 45–84.

Blake, W. K. 1970 Turbulent boundary-layer wall-pressure fluctuations on smooth and rough walls. *J. Fluid Mech.* **28**, 719–754.

Blake, W. K. 1986 *Mechanics of Flow-Induced Sound and Vibration.* Academic.

Bradshaw, P. 1967 'Inactive' motion and pressure fluctuations in turbulent boundary layers. *J. Fluid Mech.* **30**, 241–258.

Bull, M. K. 1967 Wall pressure fluctuations associated with a subsonic turbulent boundary layer. *J. Fluid Mech.* **28**, 719–754.

Bull, M. K. & Thomas, A. S. 1976 High frequency wall-pressure fluctuations in turbulent boundary layers. *Phys. Fluids* **19**, 597–599.

Choi, H. & Moin, P. 1990 On the space–time characteristics of wall pressure fluctuations. *Phys. Fluids* A **8**, 1450–1460.

Coles, D. 1969 Turbulent boundary layers in pressure gradients: a survey lecture. In *Proc. 1968 AFOSR-IFP–Stanford Conference on Computation of Turbulent Boundary Layers* (ed. D. Coles & H. Hirst). Stanford University.

DeGraaff, D. B. & Eaton, J. K. 2000 Reynolds-number scaling of the flat-plate turbulent boundary layer. *J. Fluid Mech.* **422**, 319–346.

Eckelmann, H. 1990 A review of knowledge on pressure fluctuations. In *Near-Wall Turbulence: 1988 Zoran Zaric Memorial Conference* (ed. S. J. Kline & N. H. Afgan), pp. 328–347. Hemisphere.

Emmerling, R. 1973 Translation of an extended version of *Mittielungen aus den Max-Planck-Institut fur Stromungsforschung und der Aerodynamischen Versuchsanstalt, no. 56*.

Falco, R. E. 1983 New results, a review and synthesis of the mechanism of turbulence production in boundary layers and its modification. *AIAA Paper* 83-0377.

Falco, R. E. 1991 A coherent structure model of the turbulent boundary layer and its ability to predict Reynolds number dependence. *Phil. Trans. R. Soc. Lond.* A **336**, 103–129.

Farabee, T. M. & Casarella, M. J. 1991 Spectral features of wall pressure fluctuations beneath turbulent boundary layers. *Phys. Fluids* **3**, 2410–2420.

Fershtut, A. B. 2006 On the Reynolds number dependence of passive contaminant motions in the viscous sublayer. M.S. thesis, University of Utah.

Folz, A. B. 1997 An experimental study of the near-surface turbulence in the atmospheric boundary layer. PhD thesis, University of Maryland, College Park, Maryland.

Honkan, A. & Andreopoulos, Y. 1997 Vorticity, strain-rate and dissipation characteristics in the near-wall region of turbulent boundary layers. *J. Fluid Mech.* **350**, 29–96.

Horne, M. 1989 Physical and computational investigation of the wall pressure fluctuations in a channel. PhD dissertation, The Catholic University of America, Washington, DC.

Hutchins, H. & Marusic, I. 2007 Evidence of very long meandering features in the logarithmic region of turbulent boundary layers. *J. Fluid Mech.* **579**, 1–28.

Johansson, A. V. & Alfredsson, P. H. 1983 Effects of imperfect spatial resolution on measurements of wall-bounded turbulent shear flows. *J. Fluid Mech.* **137**, 409–421.

Kenney, D. 2005 Surface vorticity flux measurements in a high reynolds number boundary layer. MS thesis, University of Utah.

Kinsler, L. E. & Frey, A. R. 1950 *Fundamentals of Acoustics.* John Wiley.

Klewicki, J. C. 1997 Self-sustaining traits of near-wall motions underlying boundary layer stress transport. In *Self-Sustaining Mechanisms of Wall Turbulence* (ed. R. L. Panton), pp. 135–166. Computational Mechanics.

Klewicki, J. C. & Falco, R. E. 1990 On accurately measuring statistics associated with small scale structure in turbulent boundary layers using hot-wire probes. *J. Fluid Mech.* **219**, 119–142.

Klewicki, J. C. & Hill, R. B. 1998 Spatial structure of negative $\partial\tilde{u}/\partial y$ in a low R_θ turbulent boundary layer. *Trans. ASME* I: *J. Fluids Engng* **120**, 773–781.

Klewicki, J. C. & Hirschi, C. R. 2004 Flow field properties local to near-wall shear layers in a low Reynolds number turbulent boundary layer. *Phys. Fluids* **16**, 4163–4176.

Klewicki, J. C. & Metzger, M. M. 2003 Studies of high Reynolds number turbulence in the atmospheric surface layer over the salt playa of western Utah. In *Reynolds Number Scaling in Turbulent Flow* (ed. A. J. Smits), pp. 45–52. Kluwer.

KLEWICKI, J. C., GENDRICH, C. P., FOSS, J. F. & FALCO, R. E. 1990 On the sign of the instantaneous spanwise vorticity component in the near-wall region of turbulent boundary layers. *Phys. Fluids* A **2**, 1497–1500.

KLEWICKI, J. C., METZGER, M. M., KELNER, E. & THURLOW, E. M. 1995 Viscous sublayer flow visualizations at $R_\theta \simeq 1500\,000$. *Phys. Fluids* **6**, 257–263.

KLEWICKI, J. C., METZGER, M. M., PERKINS, B. F. & PRIYADARSHANA, P. 2002 Reynolds number effects on wall layer convection velocities. *AIAA Paper* 02-1109.

KLEWICKI, J. C., PERKINS, B. F. & METZGER, M. M. 2005 Wall pressure statistics in a high Reynolds number turbulent boundary layer. In *Proc. Fourth Intl Symp. on Turbulent Shear Flow Phenomena* (ed. J. A. C. Humphrey, T. B. Gatski, J. K. Eaton, R. Friedrich, N. Kasagi & M. A. Leschziner), vol. 1, pp. 21–26.

KUNKEL, G. J. & MARUSIC, I. 2006 Study of the near-wall-turbulent region of the high-Reynolds-number boundary layer using an atmospheric flow. *J. Fluid Mech.* **548**, 375–402.

LAUCHLE, G. C. & DANIELS, M. A. 1987 Wall-pressure fluctuations in turbulent pipe flow. *Phys. Fluids* **30**, 3019–3024.

LONG, R. R. & CHEN, T.-C. 1981 Experimental evidence for the existence of the 'mesolayer' in turbulent systems. *J. Fluid Mech.* **105**, 19–59.

LIGHTHILL, M. J. 1963 Boundary layer theory. In *Laminar Boundary Layers* (ed. L. Rosenhead), Oxford University Press.

MCGRATH, B. E. & SIMPSON, R. L. 1987 *NASA Contractor Rep.* 4051.

METZGER, M. M. 2002 Scalar dispersion in high Reynolds number boundary layers. PhD dissertation, University of Utah.

METZGER, M. M. 2006 Length and time scales of the near-surface axial velocity in a high Reynolds number turbulent boundary layer. *Intl. J. Heat Fluid Flow* **27**, 534–541.

METZGER, M. M. & KLEWICKI, J. C. 2001 A comparative study of wall region structure in high and low Reynolds number turbulent boundary layers. *Phys. Fluids* **13**, 693–701.

METZGER, M. M., KLEWICKI, J. C., BRADSHAW, K. & SADR, R. 2001 Scaling the near-wall axial turbulent stress in the zero pressure gradient boundary layer. *Phys. Fluids* **13**, 1819–1821.

METZGER, M. M., MCKEON, B. J. & HOLMES, H. 2007*a* The near-neutral atmospheric surface layer: turbulence and non-stationarity. *Phil. Trans. R. Soc.* A **365**, 859–876.

METZGER, M., FERSHTUT, A., CAMBRON, C. & KLEWICKI, J. 2007*b* Reynolds number scaling of pocket events in the viscous sublayer. *Phys. Fluids* (under review).

MILLIKAN, C. B. 1939 A critical discussion of turbulent flows in channels and circular tubes. In *Proc. Fifth Intl Congress of Applied Mechanics*, pp. 386–392. Wiley.

MORRIS, S. C., STOLPA, S. R., SLABOCH, P. E. & KLEWICKI, J. 2007 Near surface particle image velocimetry measurements in a transitionally rough-wall atmospheric boundary layer. *J. Fluid Mech.* **580**, 319–338.

MORRISON, J. F. 2007 The interaction between the inner and outer regions of turbulent wall-bounded flow. *Phil. Trans. R. Soc.* A **365**, 683–698.

MORRISON, J. F., SUBRAMANIAN, C. F. & BRADSHAW, P. 1992 Bursts and the law of the wall in turbulent boundary layers. *J. Fluid Mech.* **241**, 75–108.

NAGUIB, A. M., GRAVANTE, S. P. & WARK, C. E. 1996 Extraction of turbulent wall-pressure time-series using an optimal filtering scheme. *Exps. Fluids* **22**, 14–28.

NATRAJAN, V. K., WU, Y. & CHRISTENSEN, K. T. 2007 Spatial signatures of retrograde spanwise vortices in wall turbulence. *J. Fluid Mech.* **574**, 155–167.

OSTERLUND, J., JOHANSSON, A., NAGIB, H. & HITES, M. 2000 A note on the overlap region in turbulent boundary layers. *Phys. Fluids* **12**, 1–4.

PANTON, R. L. 1990 Inner–outer structure of the wall-pressure correlation function. In *Near-Wall Turbulence: 1988 Zoran Zaric Memorial Conference* (ed. S. J. Kline & N. H. Afgan), pp. 381–396. Hemisphere.

PANTON, R. L. & LINEBARGER, J. H. 1974 Wall pressure spectra calculations for equilibrium boundary layers. *J. Fluid Mech.* **65**, 261–287.

PANTON, R. L. & ROBERT, G. 1994 The wavenumber-phase velocity representation for the turbulent wall-pressure spectrum. *Trans. ASME* I: *J. Fluids Engng.* **116**, 477–484.

PRIYADARSHANA, P. J. A. & KLEWICKI, J. C. 2004 Study of the motions contributing to the Reynolds stress in high and low Reynolds number turbulent boundary layers. *Phys. Fluids* **16**, 4586–4600.

Priyadarshana, P., Klewicki, J., Treat, A. & Foss, J. 2007 Statistical structure of turbulent-boundary-layer velocity–vorticity products at high and low Reynolds numbers *J. Fluid Mech.* **570**, 307–346.

Robinson, S. K. 1991 Coherent motions in the turbulent boundary layer. *Annu. Rev. Fluid Mech.* **23**, 601–639.

Sadr, R. & Klewicki, J. C. 2000 Surface shear stress measurement system for boundary layer flow over a salt playa. *Meas. Sci. Technol.* **11**, 1403–1413.

Schewe, G. 1983 On the structure and resolution of wall-pressure fluctuations associated with turbulent boundary-layer flow. *J. Fluid Mech.* **134**, 311–328.

Smith, C., Walker, J., Haidari, A. & Sobrun, U. 1991 On the dynamics of near-wall turbulence. *Phil. Trans. R. Soc. Lond.* A **336**, 131–175.

Snarski, S. R. & Lueptow, R. M. 1995 Wall pressure and coherent structures in a turbulent boundary layer on a cylinder in axial flow. *J. Fluid Mech.* **286**, 137–171.

Sreenivasan, K. R. 1989 The turbulent boundary layer. In *Frontiers in Experimental Fluid Mechanics* (ed. M. Gad-el-Hak), vol. 46, pp. 159–209, Springer.

Tsuji, Y., Fransson, H. M., Alfredsson, P. H. & Johansson, A. V. 2007 Pressure statistics and their scaling in high-Reynolds-number turbulent boundary layers. *J. Fluid Mech.* **585**, 1–40.

Wei, T., Fife, P., Klewicki, J. & McMurtry, P. 2005 Properties of the mean momentum balance in turbulent boundary layer, pipe and channel flows. *J. Fluid Mech.* **522**, 303–327.

Willmarth, W. W. & Wooldridge, C. E. 1962 Measurements of the fluctuating pressure at the wall beneath a thick turbulent boundary layer. *J. Fluid Mech.* **14**, 187–210.

Wu, Y. & Christensen, K. T. 2006 Population trends of spanwise vortices in wall turbulence. *J. Fluid Mech.* **568**, 55–76.

Wyngaard, J. C. 1969 Spatial resolution of the vorticity meter and other hot-wire arrays. *J. Sci. Instrum. (J. Phys.* E*)* **2**, 983–987.